ELSEVIER

doi:10.1016/j.ultrasmedbio.2011.02.013

● *Original Contribution*

NONSPHERICAL SHAPE OSCILLATIONS OF COATED MICROBUBBLES IN CONTACT WITH A WALL

Hendrik J. Vos,[*][1] Benjamin Dollet,[‡] Michel Versluis,[†] and Nico de Jong[*][†]

*Biomedical Engineering, Thoraxcentrum, Erasmus MC, Rotterdam, The Netherlands; [†]Physics of Fluids group, University of Twente, Enschede, The Netherlands; and [‡]Institut de Physique de Rennes, UMR 6251 CNRS/Université de Rennes 1, Campus Beaulieu, Rennes Cedex, France

Abstract—In this experimental study, the nonspherical and translational behavior of individual coated microbubbles of different sizes, in contact with a 20-μm thickness cellulose wall, are observed and categorized systematically. Images from two orthogonally positioned microscopes are merged and then recorded with an ultra-fast framing camera. Large nonspherical deformations were found with 2.25 MHz frequency ultrasound pulses having driving pressures from 80 to 325 kPa. A parametric model combining potential flow theory with a viscous boundary layer at the wall is developed and used to calculate stresses from the optically recorded microbubble oscillations. Peak shear stress of up to 300 kPa and normal stresses of up to 1 MPa are estimated when microbubbles are insonified with a 2.25 MHz pulse at 325 kPa. The clinical relevance of these results is discussed. (E-mail: n.dejong@erasmusmc.nl) © 2011 World Federation for Ultrasound in Medicine & Biology.

Key Words: Ultrasound contrast agent, Confined medium, Shape oscillations, Normal and shear stress.

INTRODUCTION

Ultrasound contrast agents (UCAs) consist of coated microbubbles and are injected into the blood circulation to image the cardiovascular system and blood perfusion. Owing to the high compressibility of gas compared with blood, microbubbles effectively scatter sound waves that are generated by the ultrasound equipment. In clinical ultrasound imaging conditions, microbubbles can compress by over 50% of the initial radius and they can expand by several factors of the initial radius (de Jong et al. 2002; Caskey et al. 2006). The expansion and compression are reduced when the microbubbles are located in confined spaces (Caskey et al. 2006, 2007; Thomas et al. 2009). Despite the large amount of literature addressing the oscillation of microbubbles in confined spaces (see Qin et al. 2009 for a review), a smaller amount can be found on the effect of the oscillation on the nearby surface. This is surprising since in therapeutic use of coated microbubbles, which is widely

investigated, it is the stress on the nearby surface of a cell membrane that is of most interest. It is known that ultrasound-driven microbubbles can open cell membranes to enhance drug and gene uptake, so called microbubble-enhanced sonoporation (Nyborg and Miller 1982; van Wamel et al. 2004; Prentice et al. 2005; Bekeredjian et al. 2005; van Wamel et al. 2006; Ohl et al. 2006; Forbes et al. 2008; Wu and Nyborg, 2008). The correlation between driving acoustic pressure amplitude and microbubble-enhanced drug uptake has been investigated by *e.g.*, Forbes et al. (2008) and Kinoshita and Hynynen (2007) but no direct correlation between the radial oscillations of microbubbles and drug uptake has been quantified so far. The reason for this is that special camera equipment is needed since the oscillation has a frequency in the order of several MHz and the framing rate should be higher than the oscillation frequency. Furthermore, special methods such as those based on time-resolved fluorescent techniques are needed to observe both the uptake of drugs or genes, and cell survival.

A neighboring surface can induce nonspherical shape deformations, micro fluidic jets and translation of the microbubble toward and away from the wall during its oscillation. From the literature, it is well-known that nonspherical shape deformations relate to the radial

---

Address correspondence to: Nico de Jong, Ph.D., Biomedical Engineering, Room Ee2302, Erasmus MC, PO Box 2040, 3000 CA Rotterdam, The Netherlands. E-mail: n.dejong@erasmusmc.nl
[1]Current address: TNO Industry and Technology, P.O. Box 155, 2600 AD Delft, The Netherlands.

oscillation amplitude (Lamb 1932; Longuet-Higgins 1989; Leighton 1994; Dollet et al. 2008; see Fig. 1 for a schematic picture of possible nonspherical shapes of a microbubble during its oscillation). At very small amplitudes (relative excursion ≤5%), the bubble predominantly keeps a spherical shape (Marmottant et al. 2006). At larger amplitudes (10%–50%), shape deformations become increasingly important, as shown both in experiments and in theory (Blake et al. 1986; Klaseboer and Khoo, 2004; Caskey et al. 2007; Qin et al. 2009). These shape deformations generally have a period-doubling effect (*i.e.*, at a one-half subharmonic) compared with the driving oscillation. When the oscillation amplitude increases further, toward a situation where the bubble radius is larger than about twice the initial radius, violent destructive effects will occur such as fragmentation (Chomas et al. 2001; Blake et al. 1986).

Several studies showed that ultrasound-driven coated microbubbles, in contact with a cellulose wall, also show nonspherical shape oscillations (Zhao et al. 2005; Vos et al. 2008; Dollet et al. 2008; Patil and Hossack 2009). Until now, no study has been performed that systematically describes the shape oscillations *perpendicular* to the wall as a function of size and driving pressure amplitude. This article gives such a systematic description and presents ultrasound conditions for which shape oscillations are significant. Since translation and the nonspherical shape oscillations have a preferential direction normal to the wall, we have adapted the classical microscope set-up to have simultaneous views of the bubble in two orthogonal planes. In addition, the observed microbubble behavior is numerically analyzed in a parametric approach to estimate the resulting normal and shear stresses on the wall. It is anticipated that these data can be useful for clarifying the relation between microbubble oscillations and sonoporation effects.

METHODS

Acoustic set-up and insonation pulses

Tone bursts were generated by an arbitrary waveform generator (AWG 8026; Tabor Electronics, Tel Hanan,
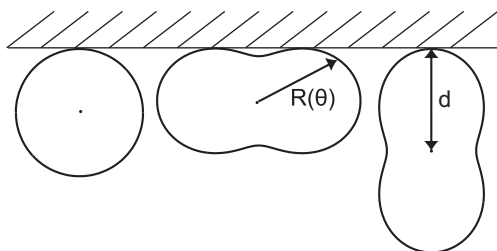

Fig. 1. Schematic drawing of surface modes of a microbubble in contact with a wall. The distance between the center of gravity and the wall is denoted by *d*.

Israel) and power amplifier (A-500; ENI, Rochester, NY, USA) that was connected to a PVDF-type focused ultrasound transducer (PA076; 2.5 cm focus, Precision Acoustics, Dorchester, UK). The transmission frequency was 2.25 MHz. Pulses typically contained six cycles, unless stated otherwise and they were Gaussian-tapered. During the experiment, microbubbles were insonified with 12 sequential pulses, having increasing amplitudes from 30 to 350 kPa peak negative pressure. Acoustic pressures were measured in a separate set-up with a calibrated hydrophone (0.2 mm PVDF; Precision Acoustics, Dorchester, UK).

Microbubbles and capillary

Experiments were performed with the non-targeting small-animal ultrasound contrast agent Targestar P (Targeson, Charlottesville, VA, USA), which consists of C_4F_{10}-filled microbubbles coated with phospholipids and an emulsifier. A diluted population (1:10000) was inserted into a cellulose capillary tube (Cuprophan, Akzo Nobel Faser AG, Germany) with 20 μm wall thickness and 160 μm inner diameter. Due to buoyancy, the microbubbles floated up to the top area of the tube. Flow in the tube was controlled with a syringe connected to a manual fine pitch micrometer screw. Microbubbles with radius ranging from 1.3 to 3 μm were positioned in the focal area of the setup.

Optical setup

Both the nonspherical shape deformations and the translation of the center of gravity of microbubbles have a preferential direction perpendicular to the wall. Therefore both cannot be imaged in the classical "top view" that is generally used in optical studies with a microscope. In this study, we add to the microscope a second microscope objective placed orthogonally to the primary objective (see Fig. 2 for a schematic drawing of the setup). The orthogonal placement was constrained by the focal distance of the microscope objectives and the physical dimensions of the objective lenses. Two 40× magnification water-immersion lenses (LUMPLFL 40×/W, N.A. 0.8; Olympus, Tokyo, Japan) were selected that have a focal distance of 3.3 mm and a lens diameter of 6.5 mm. These dimensions allow simultaneous focusing of both objectives on the region of interest, although part of the protective housing had to be machined away for both lenses to fit. A diaphragm was placed on the side view optical path to minimize optical distortion.

Microbubble oscillations were driven at a typical frequency of order MHz; the camera system should, therefore, have framing rates exceeding ten million frames per second (Mfps). We used the Brandaris-128 ultra-fast framing camera that can record two-dimensional (2-D)
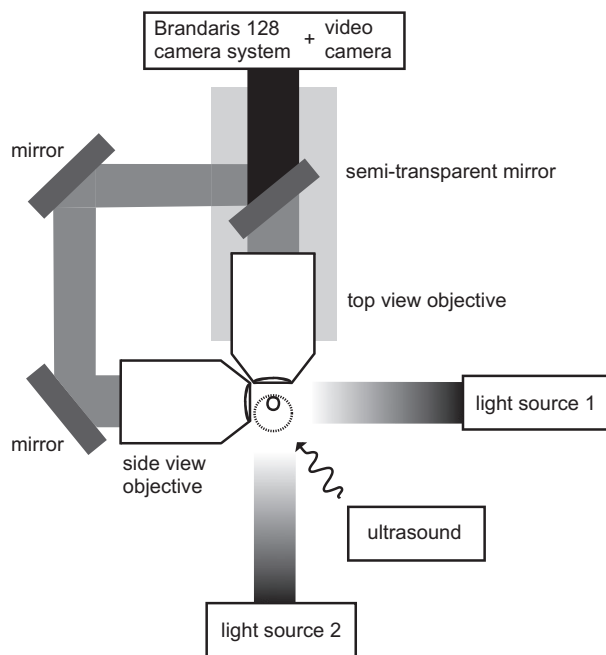
Fig. 2. Schematic drawing of the set-up showing the recombination of images of two objectives placed orthogonally.

frames at a rate of up to 25 Mfps (Chin et al. 2003). The uniqueness of the camera implies that the images from both objectives have to be merged to allow simultaneous recording of the "top view" and "side view". Therefore, the collimated optical beams from the two objectives are relayed to a semitransparent mirror where they are combined (see Fig. 2). The two objective lenses are mounted each on a separate manual precision stage.

In standard mode, the Brandaris-128 camera records six movies of 128 frames. In this study, the camera system was used in a segmented mode, thus, dividing the frame sequence in two separate segments of 64 frames each providing 12 movies per experiment (van der Meer et al. 2007). The choice of six cycles at 2.25 MHz in combination with the recording time of the camera system (∼5 μs) allowed us to record the entire microbubble oscillation and the initial and final resting size, which are needed for a correct analysis and plotting of the data. The pixel size was $0.17 \times 0.17 \ \mu m^2$, which was sufficient to accurately resolve the bubble shape.

Simultaneously with the ultra-fast framing recordings, the side view was monitored with a regular video camera (Wat 902-H; Watec, Orangeburg, NY, USA) operating at 30 fps. The frames were digitized and stored to a personal computer.

Image processing and data analysis

To quantify the nonspherical shape deformations, a spherical harmonic decomposition was applied as described in Vos et al. (2008). Edge detection of the

bubble in both side view and top view using a minimum cost algorithm as described in van der Meer et al. (2007) resulting in the bubble contour $R(\theta)$. The minimum cost algorithm was applied twice on the same microbubble image. In the first iteration, the center of mass (c.o.m.) of the bubble is obtained; in the second iteration, the final circumference is tracked around the measured c.o.m. Decomposition of the circumferential shape into spherical harmonic amplitudes A_n, $n = 0$ and 2, was achieved using

$$A_n = \left(n+\frac{1}{2}\right)\int_0^\pi R(\theta)P_n(\cos\theta)\sin\theta \ d\theta$$

where P_n represents the Legendre polynomial of degree n and zero order. Note that a zero-order spherical harmonic shape assumes cylindrical symmetry around the axis perpendicular to the wall, which we will validate by the spherical symmetry of the bubble seen in top view. In the present configuration, a positive value of A_2 denotes an oblate (flattened) shape and a negative value denotes a prolate (elongated) shape with respect to the wall. The value of A_1, the translation mode, is always zero because in the description used here the origin of $R(\theta)$ is equal to the center of mass. The distance of the c.o.m. to the wall is denoted by d. Note that if the oscillation is purely spherical and the bubble is touching the wall, then $d(t) = A_0(t) = R(t)$. Since the volume of the microbubble is given by $V = 4/3\pi A_0^3$, we denote oscillations in A_0 as oscillations in the "breathing mode," or as the radial response, throughout this text.

From the analysis of many recordings, we estimate a root-mean-square noise level of 0.15 μm in $A_0(t)$, $d(t)$ and $A_2(t)$ in a frequency band of 0 Hz to $f_{Nyquist} \approx 7.5$ MHz. The value of A_3 and higher spherical harmonic modes generally show root-mean-square levels below the noise level. We, therefore, truncate the spherical harmonics series at $n = 2$ when describing the bubble shapes.

RESULTS

Individual bubble analysis

Figure 3 shows selected frames from a recording of a 2.3 μm radius bubble. The bubble was insonified with a pressure level of 270 kPa and a frequency of 2.25 MHz. The camera recorded at a frame rate of 15.3 Mfps corresponding to an interframe time of 65 ns. Full frames were cropped to two subframes of 108 × 108 pixels, showing both the top view and side view of the bubble.

Frame zero in Fig. 3 shows the initial shape of the bubble and frames 1 to 15 depict the bubble oscillations. The selected frames start at the third cycle of the bubble
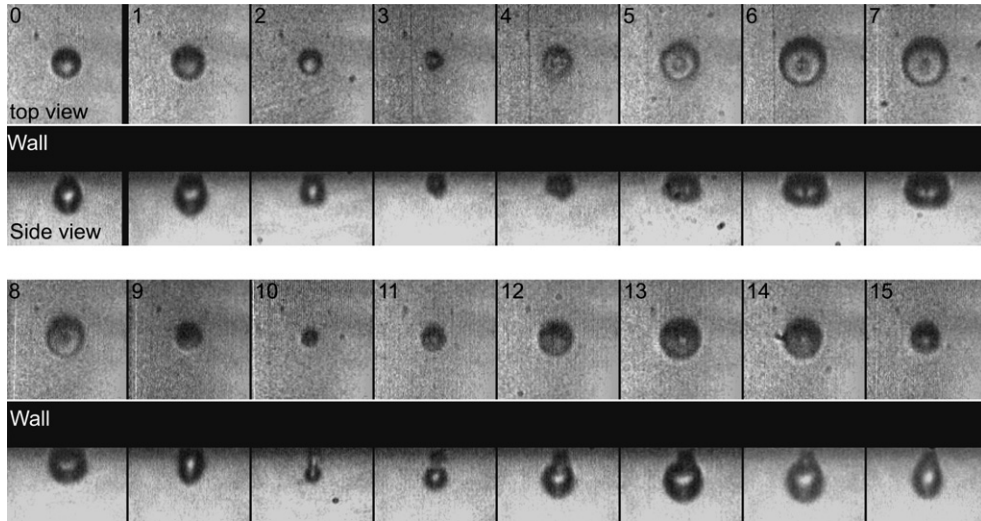
Fig. 3. Selected frames from the recording of a bubble with a radius of 2.3 μm. Top rows show the top view of the bubble and lower rows show the same bubble in a side view, at the same moment. Ultrasound excitation pulse has 270 kPa amplitude, f = 2.25 MHz. Sampling time is 65 ns.

oscillation and the sequence lasts for two cycles. The top view shows a spherical shape throughout, while the side view clearly shows nonspherical shapes of the vibrating bubble. A closer look at frames 5 to 7 reveals an apparent toroidal shape of the bubble. Frames 9 to 12 show an elongated shape with respect to the wall. Strikingly, in the top view images a toroidal shape (frame 7) appears larger than the elongated shape (frame 15) even though the volume of the microbubble is the same for frame 7 and frame 15. Furthermore, the side-view images show that the vibrating bubble stays in contact with the wall.

The bubble contour was traced and decomposed into spherical harmonic amplitudes using eqn (1). Figure 4 shows the A_0, A_2 and d, the position of the c.o.m. relative to the wall, as a function of time. The microbubble was insonified at a pressure of 200 kPa (Fig. 4a) and 270 kPa (Fig. 4b) and with a frequency of 2.25 MHz. In Fig. 4a, the A_0 oscillations shows a relative amplitude of 22% (calculated by (1/2 $\times$ peak-to-peak excursion)/ R_0). The relative amplitudes of d and A_2 are up to 25% and 17%, respectively, in side view. By definition, a larger value of d corresponds to a bubble that has moved down, away from the tube wall. Detailed analysis using the Hilbert transform of the signal showed that A_0 and d oscillate in phase. The use of the above phase shift between oscillation and translation could potentially be used to determine the acoustic microstreaming around an oscillating microbubble (Marmottant et al. 2006). However, no conclusive data on the phase shift between A_0 (t) and A_2 (t) can be given because of noise and instability in the
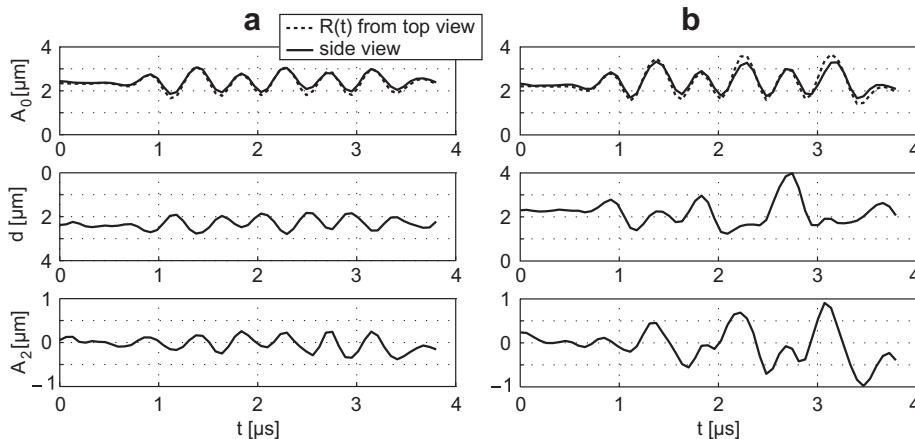

Fig. 4. Time evolution of microbubble shape and position obtained from top-view and side-view analysis. Top: volumetric mode A_0; Middle: distance of the bubble center to the wall d; Bottom: shape mode A_2. Pressure amplitude was 200 kPa (left panel) and 270 kPa (right panel), the frequency was 2.25 MHz and pulses contained six cycles.

derived signals. Possible microstreaming and related stresses on the wall caused by the oscillating and translating microbubble will be addressed in a later section.

Insonation at an amplitude of 270 kPa (Fig. 4b) leads to a relative amplitude A_0 of 52%. The $d(t)$ curve shows more complex behavior. In the first cycle, $d(t)$ roughly follows the radial excursion (like in Fig. 4a). In subsequent cycles, a period-doubling response increasingly dominates the overall curve, while a small fundamental frequency component is still visible. The peak-to-peak displacement of the bubble center is almost 3 μm, which is large compared with the initial radius of 2.3 μm. At $t = 2.7$ μs, d is momentarily larger than A_0. Frame 11 in Fig. 3, corresponding to this time instance, shows that the microbubble is momentarily split up in two smaller bubbles: the larger bubble is far from the wall and a smaller bubble is in contact with the wall. Four frames later the two bubbles have coalesced into a single bubble that is again in full contact with the wall. The contour tracking algorithm cannot track two different bubbles in the same frame but rather produces a closed contour around both bubbles. Hence, the values of A_0, d and A_2 at $t = 2.7$ μs may be slightly underestimated in Fig. 4b at that time instance.

The top view recordings show a spherical shape throughout the oscillations, from which we conclude that the axis of symmetry is indeed normal to the wall. As already addressed in Vos et al. (2008), an A_2 shape oscillation can produce a subharmonic component in top view in the radius-time curve, which could be erroneously interpreted as a volumetric subharmonic oscillation. The period-doubling response is also visible in the A_0-oscillation observed in side view but it is not the dominant contribution. The radial subharmonic oscillation amplitude observed in top view ($R(t)$ in Fig. 4a) is about 25% higher than that of A_0 observed in side view.

In a second experiment, the single bubble was excited with 12 pressure pulses with increasing pressure levels ranging from 30 to 300 kPa. The amplitudes of oscillation of the three parameters (A_0, d and A_2) are plotted as a function of the excitation pressure (see Fig. 5). The amplitude of oscillation was obtained by taking the maximum of the envelope of the time traces.

The amplitudes of oscillation of the three parameters show an increase with increasing driving pressure level. Furthermore, the amplitude of d is marginally smaller than the amplitude of the A_0 oscillation up to a driving pressure level of 230 kPa. This means that the oscillatory translation of the center of mass is significant, as also observed in Fig. 3. Also, the amplitude of oscillation of A_2 is roughly half of that of A_0, up to a driving pressure level of 200 kPa. This means that the nonspherical shape deformations are also significant. Remarkably, at 240 kPa and 270 kPa, when the bubble shows additional subhar-
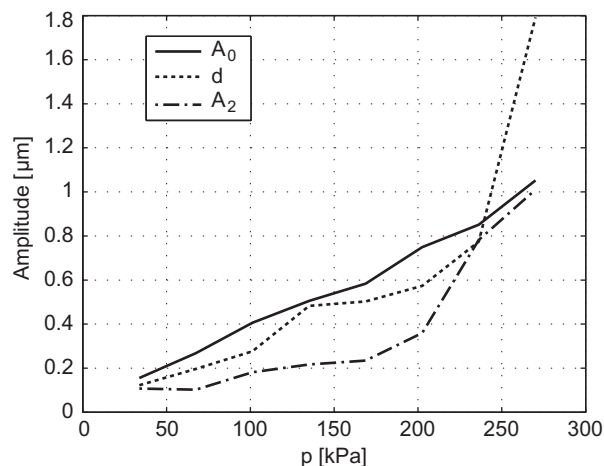

Fig. 5. Amplitude of radial mode oscillation (A_0), distance d and second order spherical harmonic (A_2) as a function of pressure. Frequency 2.25 MHz, microbubble initial radius of 2.3 μm.

monic response (Fig. 4b), the amplitude of oscillation of d becomes higher than that of A_0.

Fundamental-frequency response

Twenty differently-sized bubbles were subjected to similar analysis as described above and generalized results are obtained. Since we are interested in both the fundamental-frequency response and the observed period-doubling effects, the time curves of A_0, d and A_2 were band-pass filtered to obtain a response at the fundamental frequency and at the subharmonic frequency. The amplitude of the filtered responses is then obtained by taking the maximum of the Hilbert transform of the filtered curves. Figure 6 shows the amplitude of A_0 and d at the fundamental frequency as a function of radius and insonation pressure. The amplitude of oscillation vs. radius and pressure is coded in gray-scale. White denotes the lowest amplitude and black the highest amplitude. For some combinations of size and pressure, no reliable data were available because of either fragmentation or fast deflation caused by the ultrasound.

At an insonation pressure larger than 100 kPa, the maximum response of A_0 is seen for microbubbles with a radius of 1.8 μm, which will be referred to as the resonant size of these bubbles at 2.25 MHz. This value is within the range of those found in the literature for phospholipid-coated microbubbles (Chomas et al. 2002; van der Meer et al. 2007; Vos et al. 2011).

A relative comparison between the oscillation amplitude of A_0 and d can be made based on the dataset. At any point in the experimental radius-pressure domain depicted in Fig. 6, the ratio between $|A_0|$ and $|d|$ is 0.6 on average, and always within the range 0.5–0.7. For a spherically symmetric oscillation, a unit value is expected.
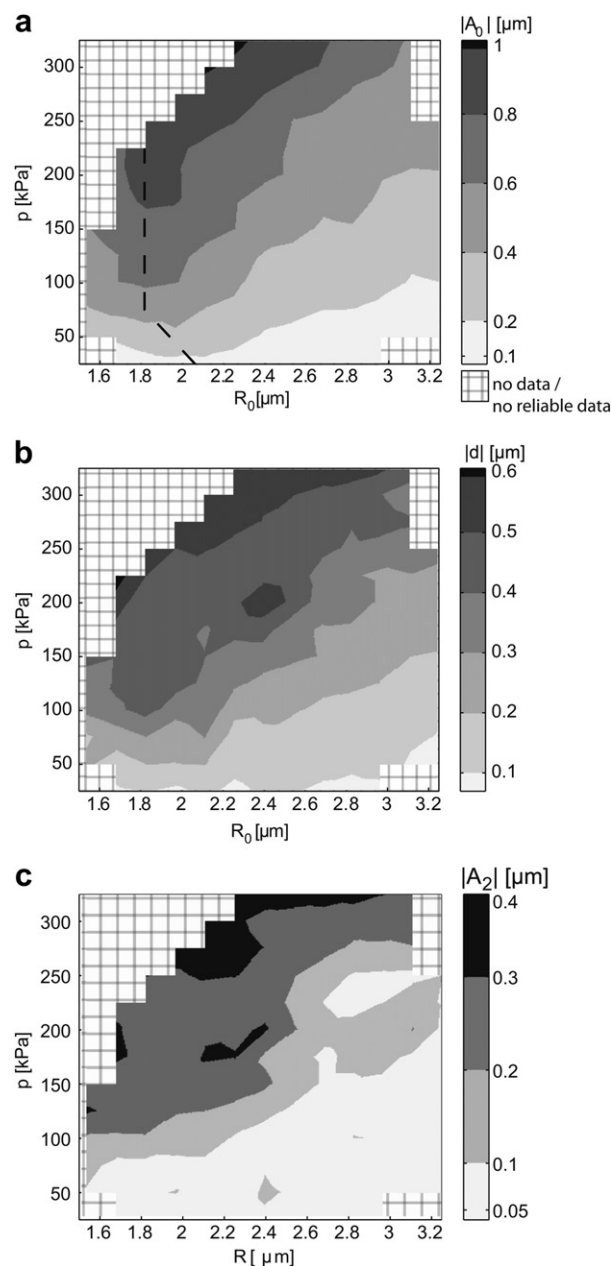
Fig. 6. Amplitudes of the fundamental frequency oscillation of (a) A_0; (b) d; and (c) A_2 as a function of pressure and initial radius. The dashed line in (a) denotes the radius of maximum response as a function of pressure. The values are obtained from 20 different bubbles (188 recordings).
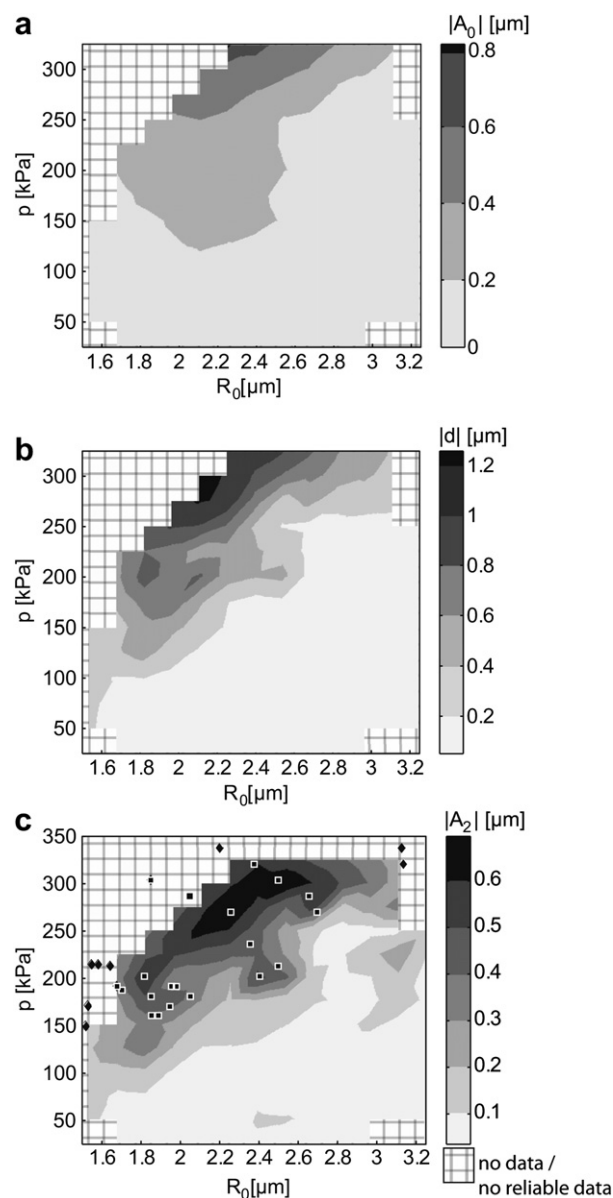

Fig. 7. Amplitudes of the subharmonic oscillation of (a) A_0; (b) d; and (c) A_2 as a function of pressure and initial radius: (c) also contains squares to denote the occurrence of jets, and diamonds to denote the occurrence of fragmentation.

Comparison of Fig. 6c with Fig. 6a shows that the ratio between A_2 at the fundamental frequency and A_0 is between 0 and 0.5.

Subharmonic response

The amplitudes of A_0, d and A_2 at the subharmonic frequency (*i.e.*, 1.125 MHz) are shown in Fig. 7. The amplitude of subharmonic oscillation of A_0 (Fig. 7a) is

below 0.2 μm for a large range of combinations of R_0 and p. The overall maximum is 0.8 μm, corresponding to microbubbles with a radius of 2.3 μm excited by 325 kPa pulses. For insonation pressures between 100 kPa and 250 kPa, the largest subharmonic response is found for microbubbles with an initial radius $R_0 = 2.1$ μm. Figure 7b and c generally show similar behavior. Microbubbles with an initial radius of 1.8 to 2.2 μm show much larger amplitude of subharmonic oscillation in d and A_2 than larger and smaller microbubbles. Moreover, a nonlinear relation exists between the amplitude of

subharmonic oscillation and the insonation pressure. For example, microbubbles with radius of 1.8 μm show an A_2 amplitude of 0.1 μm when excited with an acoustic pressure of 80 kPa and 0.4 μm amplitude when excited by double acoustic pressure, 160 kPa. In addition, microbubbles with larger radii show a threshold for the subharmonic response. For example, microbubbles with a radius of 2.8 μm show a relatively low subharmonic effect for pressures below 250 kPa but the amplitude is doubled for a pressure of 300 kPa.

As stated before, the occurrence of surface modes might bias the radial dynamics that is seen in a classical top view microscope setup. Based on the current dataset, it can be shown that the subharmonic radial oscillation (A_0) observed in top view is typically overestimated by 5% to 20%. When the occurrence of nonsphericity (A_2 modes and higher) is even higher, *i.e.*, where the A_2 mode shows amplitude larger than 0.6 μm (corresponding to $R = 2.4$ μm, $p = 300$ kPa), the subharmonic amplitude observed in top view is overestimated by 80% compared with the subharmonic amplitude seen in side-view.

Deflation and fragmentation

When the oscillation amplitude becomes large, *i.e.*, on the order of 50% of the initial bubble radius, microbubbles partially deflate within the duration of one pulse. The exact mechanisms leading to deflation during excitation are currently unknown (Borden et al. 2005; Guidi et al. 2010), although it can be hypothesized that lipid shedding reduces the amount of surfactants on the surface; hence, increases surface tension, leading to a build-up of Laplace pressure; hence, to gas dissolution. Bubbles may also fragment. Fragmentation is a process in which the initial microbubble is split into multiple smaller microbubbles (Chomas et al. 2001). Fragmentation prevents a reliable contour tracking and deflation leads to an ambiguous estimate of the equilibrium radius, and the recordings showing either of the two is excluded from the dataset represented in Figs. 6 and 7. The exclusion area is filled with coarse gridlines. Comparison of the location of the destructive and nondestructive areas shows that smaller bubbles insonified at high pressure are destroyed; this observation is consistent with the findings described earlier by Chomas et al. (1999, 2001, 2002). The destruction threshold reported by Chomas et al. (2001) correlates well with the upper-left boundary between the destructive and nondestructive area in Figs. 6 and 7.

We regularly found that the high-amplitude nonspherical shape modes lead not only to a transitory breakup of the microbubble (cf. Fig. 3, frames 10 and 11) but also to a persistent fragmentation into two separate bubbles. The one bubble stays in contact with the wall while the other is located at a distance of 5 to 10 μm from the wall. This effect was observed earlier by Zhao et al. (2005). The current side view recordings are manually scored and the data is drawn in Fig. 7c (diamonds) at the location where nonreversible bubble breakup occurs (N = 8). As expected, the diamonds are located in the destructive area. We have noted that the highest chance of nonreversible bubble breakup is observed for a radius between 1.5 and 1.7 μm and an insonation pressure of 150 to 220 kPa. This is close to the nondestructive area where the relative amplitude of the second order surface mode (A_2 / R_0) is very high and a relation between large surface deformations and eventual breakup was previously proposed (see for example Leighton 1994; Chomas et al. 2001; Palanchon et al. 2005).

During some recordings, the side-view image was also recorded with the 30 fps video camera. In these recordings, the freely floating bubble that was formed after the bubble breakup was seen to survive for at least 1 s while dragged away by residual flow in the capillary. The radius was near 0.5 μm. Uncoated bubbles, despite the relatively insoluble gas, would not survive for such a long time, therefore, the pinched-off bubbles are believed to have a phospholipid coating inherited from the original microbubble.

Jetting

Figure 3 shows a central spot within the bubble in top view (frames 4–7). Careful observations of the side-view images reveal a thin dark line, with a width of hundreds of nanometers. The line was visible despite a size close to the expected optical diffraction limit of the microscope and camera system. The combination of observation of the spot and the thin line leads us to believe that this is a microjet (Benjamin and Ellis 1966; Crum 1979; Lauterborn 1982; Zhao et al. 2005; Postema et al. 2005; Ohl et al. 2006). The recordings were manually scored for the occurrence of such a jet and the results are plotted in Fig. 7c (N = 22). A high correlation with the A_2 modes was observed. Moreover, it was observed that the occurrence of such jets does not necessarily indicate instantaneous microbubble destruction.

Wall attractions

An oscillating bubble can be significantly attracted toward a wall, tentatively called the "Narcissus" effect by Marmottant et al. (2006). The effect can be modeled by a secondary radiation force between the bubble and its so-called "image bubble". The image bubble is a replica of the microbubble at the mirrored position on the other side of the wall (Howkins 1965; Plesset and Prosperetti 1977; Leighton, 1994; Harkin et al. 2001; Cui et al. 2006; Marmottant et al. 2006; Doinikov et al. 2009). For a bubble already in contact with the wall,

the attraction could mean that the bubble flattens during the oscillation. The attraction stops after the oscillation and capillary forces should bring the microbubble back to a spherical shape. To investigate the significance of wall attraction and possible flattening of coated microbubbles, a 2.3 μm bubble was insonified with 2.25 MHz tone bursts of eight cycles and a pressure amplitude of 240 kPa. The bubble was imaged in side-view and the camera operated in its regular mode, providing 128 frames per recording and it operated at relatively low framing rate ($\sim$8.5 Mfps), providing a relatively long recording time (14 μs) to resolve a possible attraction and recovery of the bubble's position.

Figure 8 shows the radial oscillation, the position of the center of mass, and the A_2 oscillation of the microbubble. The driving pulse reaches the microbubble at $t = 0.8$ μs. The second oscillation in Fig. 8a starting at $t \approx 7.5$ μs is due to the reflection of the pulse at the surfaces of the microscopic lenses. The initial distance d is 2.3 μm (Fig. 8b), equal to the initial radius, as expected since the microbubble is spherical and in contact with the wall. During the first cycles of the oscillation, the period-averaged distance d decreases, and within 1 μs ($\sim$2 cycles), it reaches an overall smaller
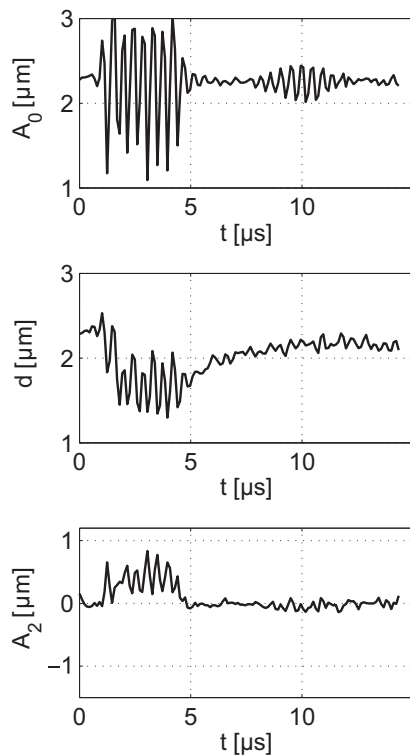

Fig. 8. Oscillation of A_0 (top); d (middle); and A_2 (bottom) as a function of time of a 2.5 μm radius bubble. The driving pressure contained eight cycles at 2.25 MHz at a pressure level of 240 kPa.

value at average. After the insonation, d returns to its initial value with a time constant of about 3 μs. Analysis of the shape showed that the period-averaged bubble size, in terms of A_0, was not smaller during or after the insonation. Yet, a non-zero value of A_2 showed that the bubble has obtained an oblate shape on average during oscillation, in accordance with the smaller value of d seen in the figure during oscillation. These observations confirm the significant attractive force exerted by the wall on the bubble during oscillation.

Parametric estimate of normal and shear stress

Evaluation of the normal and shear stress exerted by the microbubble on the wall may give important insight in the physical phenomena that ultimately lead to cell membrane permeation. *In situ* measurements of local shear and normal stress at the wall are extremely challenging. On the other hand, the experimental results presented in this article can be converted into shear and normal stresses in a parametric approach. This method is exploited in the current section.

The model used for the parametric approach is shown in the Appendix. It assumes a single microbubble in contact with a rigid wall. The bubble shape is described by spherical harmonics with an axis of symmetry normal to the wall. The fluid is assumed inviscid except for a boundary layer in the vicinity of the wall. A no-slip boundary condition at the wall is used. The potential flow around a bubble undergoing volumetric oscillations, translation and nonspherical deformation is calculated which then leads to the calculation of the normal and shear stresses. Since it is a parametric model, the optically recorded microbubble dynamics $A_0(t)$, $d(t)$ and $A_2(t)$ act as input. The model has not been validated until now and the results should therefore be considered preliminary.

Figure 9 shows results obtained with the parametric approach. The recorded microbubble had an initial radius of 2.1 μm and the insonation pressure was 180 kPa. The bubble was oscillating in the regime where a period-doubling A_2 surface mode and translation was present (see Fig. 9a for the time curves of A_0, d and A_2).

The calculated shear stress at the wall varies as a function of time and lateral distance r from the axis of symmetry. The shear stress has a stagnation point at $r = 0$ for reasons of symmetry of the problem and also at $r \rightarrow \infty$ where the perturbation by the bubble has vanished. For these specific bubble and oscillations, a maximum peak value of the shear stress was found at $r = 0.65$ μm; Fig. 9b shows the time dependency of the shear stress at that distance. For convenience, a trend line was added (dotted line) that was obtained by low-pass filtering of the original shear stress curve. Strikingly, a steady non-zero shear stress is seen after three cycles of the original frequency. The non-zero shear stress is
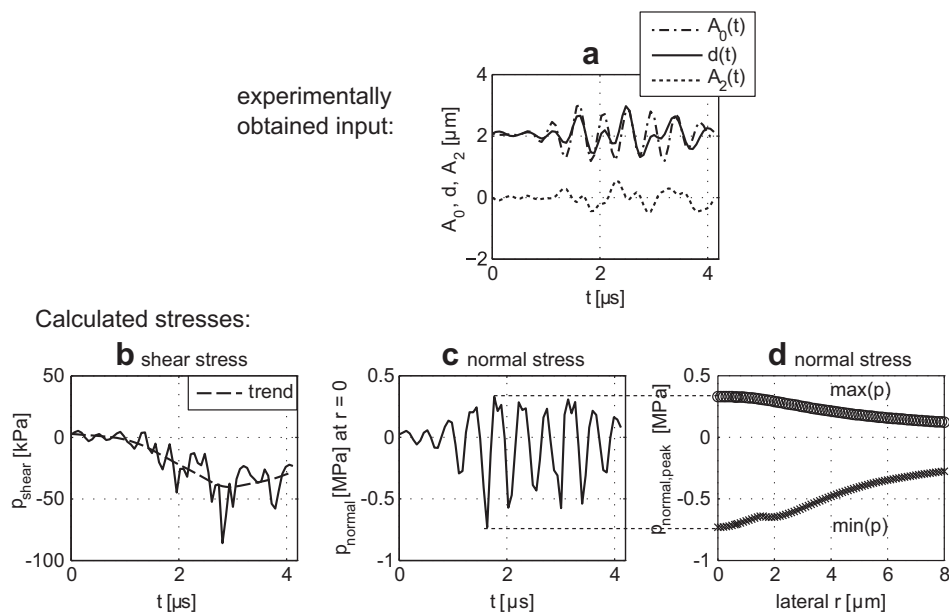
Fig. 9. Parametrically calculated stresses caused by an oscillating microbubble in contact with the wall. (a) Time traces of A_0, d and A_2 obtained from the recording of the microbubble; (b) time trace of the calculated shear stress at the wall at an lateral distance of $r = 0.65$ μm; (c) time trace of the normal stress; (d) peak normal stresses as a function of lateral distance. The initial radius of the bubble was 2.1 μm, the insonation pressure was 180 kPa.

caused by a fluid motion regularly denoted as micro-streaming around an oscillating bubble (Marmottant and Hilgenfeldt 2003). Moreover, the microstreaming gradually develops, which means that the shear stresses have higher peak-values after some initial cycles than during the initial cycles.

Figure 9c shows the time trace of the normal stress on the wall at $r = 0$ and Fig. 9d shows the peak-positive and peak-negative values of the time traces of the normal stress as a function of r. The maximum normal stresses are found at $r = 0$, which is expected since the wall motion of the microbubble with respect to the wall is highest at $r = 0$. It is also observed that the peak-negative pressure is generally larger than the peak-positive pressure. The bubble is more "pulling" than "pushing" at the wall.

The parametric analysis is repeated for all micro-bubble recordings. The results are summarized in Fig. 10, showing as a function of microbubble radius and driving pressure: (a) the maximum observed peak-positive normal stress; (b) the maximum observed peak-negative normal stress; (c) the maximum observed shear stresses; (d) the observed steady shear stresses during the final cycles of the insonation pulse. Since the results from the parametric stress estimate should be considered preliminary, we are not going to discuss details found in these plots. Yet, general trends observed in Fig. 10 will be discussed in the next section.

DISCUSSION

General observations

The combination of the orthogonal microscope and an ultra-fast framing camera provides a unique tool for studying the behavior of ultrasound contrast agent micro-bubbles in contact with a wall. We observed nonspherical shape deformations of phospholipid-coated microbubbles insonified at clinically relevant frequencies and pressures. This is consistent with findings earlier reported in litera-ture (Zhao et al. 2005; Dollet et al. 2008; Vos et al. 2008). Nonspherical shape oscillations were observed that lead to a subharmonic frequency component in A_0 and d. The radius where the nonspherical shape oscillations have lowest threshold (1.8 μm–2.2 μm) is close to the resonant radius (1.8 μm) at 2.25 MHz. This is consistent with the theory of parametrically driven nonspherical shape oscillations that are coupled to volumetric oscillations (Lamb 1932; Blake et al. 1986; Longuet-Higgins 1989; Brenner et al. 1995), which shows the equivalence between the radius of maximum radial response at the *fundamental* frequency (1.8 μm in our case) and the radius with maximum amplitude of *period-doubling* surface modes (1.8 μm–2.2 μm in our case). The theory states that the energy stored in the fundamental-frequency volumetric oscillations feeds shape instabilities but a certain amount of energy is needed for a shape instability to grow. Therefore, shape
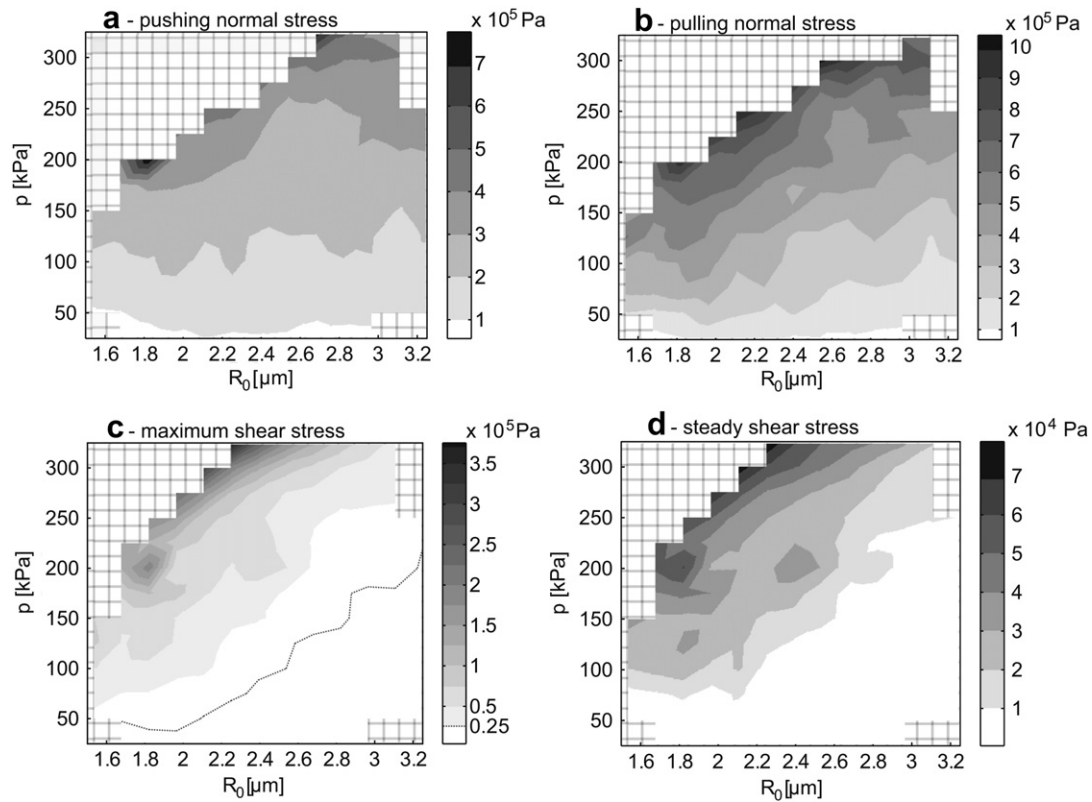
Fig. 10. Stresses acting on the wall calculated with the parametric approach: (a) peak-positive normal stress (pushing); (b) peak-negative normal stress (pulling); (c) Maximum shear stress; (d) steady shear stress during the final part of the insonation. The dotted line is the 2.5 10^4 Pa contour.

instabilities are most present if the microbubble is driven near resonance. However, volumetric oscillations (A_0) are to first order independent of shape instabilities (Longuet-Higgins 1989) and the theory, therefore, does not explain the subharmonic oscillations found in A_0. It is generally assumed that a *volumetric* subharmonic response is highest when the transmission frequency is near two times the resonance frequency (Prosperetti 1975; Eller and Flynn 1969; Sun et al. 2005). According to van der Meer et al. (2007), a resonance frequency of 1.125 MHz would then correspond to a resonant radius for the subharmonic near 4.3 μm, not 2.1 μm. Unfortunately, bubbles with a radius of around 4.3 μm that may show volumetric sub-harmonic oscillations, were out of range in the current experiments. An experimental study of the volumetric subharmonic behavior of coated single microbubbles is reported by Sijl et al. (2010). The current observations of the subharmonic behavior of A_0 may be explained by a coupling of energy from the surface modes into the volumetric mode. Such a coupling is predicted by Longuet-Higgins (1989) for uncoated gas bubbles in an unbound medium although it is predicted to be small.

An A_2 shape mode with its axis of symmetry normal to the wall will bias the analysis of the microbubble volumetric oscillations in observations with a top view microscope.

The value of A_2 was seen to be relatively low for excitation pressures below 100 kPa (see Fig. 7) in the current experimental conditions. This excitation pressure corresponds to a maximum radial excursion of 30% of the initial radius (see Fig. 6). Therefore, a relative radial excursion of 30% may act as a threshold indicator for A_2 mode oscillations and, consequently, to a first approximation whether the top view microscope analysis could be biased.

Literature shows that a period-doubling surface mode grows in time until the forcing equals the damping of the surface mode, at which point the oscillation amplitude saturates (Longuet-Higgins 1989; Dollet et al. 2008). The time traces in Fig. 4b show such a growth in time. Further analysis of the data set shows that the time from start to saturation can also be as short as 1 μs, that is, two cycles of the driving pressure pulse. Thus, the duration of the exciting acoustic pulse, six cycles in the currently reported experiments, may have an effect on the final amplitudes of oscillation of A_0, d and A_2 reported in Figs. 5–7 although quantification of the effect is not possible from this particular data set.

Parametric stress estimate

Some general results can be extracted from the data plotted in Fig. 10. The first result is that the pulling forces

on the wall are larger than the pushing forces; this is consistent with the data on bubble-cell interactions shown by van Wamel et al. (2004) where a cell membrane excursion is higher during the compression phase of the oscillation of a nearby microbubble. The amplitude of the normal stress at the wall is up to a factor of 5 higher than the insonation pressure, which can be explained by the resonant nature of microbubbles that increases the local energy density.

The second result is that the shear forces are larger than reported in literature for nondestructively oscillating contrast agent microbubbles. The order of magnitude, 25–350 kPa, is higher than the values calculated by *e.g.*, Forbes et al. (2008) and Wu et al. (2002) that mention shear stresses of 17 kPa and 9 kPa, respectively. Possible explanations for the difference could be that the current model uses experimental time traces as input and it incorporates bubble translation and shape modes, which were neglected in the calculations by Forbes et al. (2008) and Wu et al. (2002).

The third result is that for any given radius in the experimental range, up to about pressures of 150 kPa, the normal and shear stresses relate linearly to the insonation pressure. For higher insonation pressures, the stresses increase more than linear with the insonation pressure, *i.e.*, the stresses show highly nonlinear relation with the insonation pressure. This suggests that the excitation pressure should be precisely controlled in microbubble experiments where shear stress is the key parameter.

Clinical relevance

The estimated values of normal and shear stresses are much higher than those exerted by blood flow. Shear stress from blood flow is on the order of 1 Pa, while the microbubble is estimated to produce shear stresses on the order of 100 kPa. Blood pulsation leads to pressure variations of around 5 kPa while the oscillating microbubble produces up to 1 MPa pressure. There is, however, a difference in time scale: the large stresses from microbubbles only act for microseconds while stress from blood flow acts on the order of a second. No conclusions can, therefore, be drawn from a direct comparison of values. On the other hand, ultrasound settings in the same range as those used in the current experiments lead to sonoporation (Qin et al. 2009; Forbes et al. 2008). This suggests that the side-view microscope, in combination with the parametric model, can provide useful information about the interaction of oscillating microbubbles with cells.

Microjetting occurs frequently at pressures that are in the diagnostic range. The formation of jets seems to coincide with surface instabilities and a subharmonic oscillation of A_0. Acoustic measurements of the subharmonic sound emission during sonoporation experiments may therefore provide a tool for monitoring surface instabilities, and hence, for possible microjetting phenomena. Furthermore, a jet will probably produce a frequency-rich echo that also may be recorded. Since the occurrence of jets induced by surface instabilities has a period-doubling nature with respect to the driving ultrasound, the periodicity of the frequency-rich emission can discriminate between regular higher harmonic sound emission from microbubbles and the impulsive sound of a microjet.

REFERENCES

Bekeredjian R, Grayburn PA, Shohet RV. Use of ultrasound contrast agents for gene or drug delivery in cardiovascular medicine. J Am Coll Cardiol 2005;45:329–335.

Benjamin TB, Ellis AT. The collapse of cavitation bubbles and the pressures thereby produced against solid boundaries. Phil Trans R Soc Lond A 1966;260:221–240.

Benjamin TB, Ellis AT. Self-propulsion of asymmetrically vibrating bubbles. J Fluid Mech 1990;212:65–80.

Blake JR, Taib BB, Doherty G. Transient cavities near boundaries. Part 1. Rigid boundary. J Fluid Mech 1986;170:479–497.

Borden MA, Kruse DE, Caskey CF, Zhao S, Dayton PA, Ferrara KW. Influence of lipid shell physicochemical properties on ultrasound-induced microbubble destruction. IEEE Trans Ultrason Ferroelectr Freq Control 2005;52:1992–2002.

Brenner MP, Lohse D, Dupont TF. Bubble shape oscillations and the onset of sonoluminescence. Phys Rev Lett 1995;75:954–957.

Caskey CF, Kruse DE, Dayton PA, Kitano TK, Ferrara KW. Microbubble oscillation in tubes with diameters of 12, 25, and 195 microns. Appl Phys Lett 2006;88:033902.

Caskey CF, Stieger SM, Qin S, Dayton PA, Ferrara KW. Direct observations of ultrasound microbubble contrast agent interaction with the microvessel wall. J Acoust Soc Am 2007;122:1191–1200.

Chin CT, Lancée CT, Borsboom JMG, Mastik F, Frijlink ME, de Jong N, Versluis M, Lohse D. Brandaris 128: A 25 million frames per second digital camera with 128 highly sensitive frames. Rev Sci Instr 2003; 74:5026–5034.

Chomas JE, Dayton PA, Allen JS, Morgan KE, Ferrara KW. Mechanisms of contrast agent destruction. IEEE Trans Ultrason Ferroelectr Freq Control 2001;48:232–248.

Chomas JE, Dayton PA, May DJ, Ferrara KW. Nondestructive subharmonic imaging. IEEE Trans Ultrason Ferroelectr Freq Control 2002;49:883–892.

Chomas JE, Dayton PA, Morgan KE, Allen JS, Ferrara KW. Optimization of microbubble destruction. IEEE Ultrason Symp 1999;2: 1689–1692.

Crum LA. Surface oscillations and jet development in pulsating bubbles. Journal de Physique (Paris) 1979;(Suppl to 11):c8–285.

Cui J, Hamilton MF, Wilson PS, Zabolotskaya EA. Bubble pulsations between parallel plates. J Acoust Soc Am 2006;119:2067–2072.

de Jong N, Bouakaz A, Frinking P. Basic acoustic properties of microbubbles. Echocardiography 2002;19:229–240.

Doinikov AA. Translational motion of a bubble undergoing shape oscillations. J Fluid Mech 2004;501:1–24.

Doinikov AA, Zhao S, Dayton PA. Modeling of the acoustic response from contrast agent microbubbles near a rigid wall. Ultrasonics 2009;49:195–201.

Doinikov AA. Translational motion of two interacting bubbles in a strong acoustic field. Phys Rev E 2001;64:026301.

Doinikov AA, Bouakaz A. Theoretical investigation of shear stress generated by a contrast microbubble on the cell membrane as a mechanism for sonoporation. J Acoust Soc Am 2010;128:11–19.

Dollet B, van der Meer SM, Garbin V, de Jong N, Lohse D, Versluis M. Nonspherical oscillations of ultrasound contrast agent microbubbles. Ultrasound Med Biol 2008;34:1465–1473.

Eller AI, Flynn HG. Generation of subharmonics of order one-half by bubbles in a sound field. J Acoust Soc Am 1969;46:772–727.

Feng ZC, Leal GL. Translational instability of a bubble undergoing shape oscillations. J Fluid Mech 1995;7:1325–1336.

Forbes MM, Steinberg RL, O'Brien WD Jr. Examination of inertial cavitation of Optison in producing sonoporation of Chinese hamster ovary cells. Ultrasound Med Biol 2008;34:2009–2018.

Garbin V, Dollet B, Overvelde M, Cojoc D, Di Fabrizio E, van Wijngaarden L, Prosperetti A, de Jong N, Lohse D, Versluis M. History force on coated microbubbles propelled by ultrasound. Phys Fluids 2009;21:092003.

Guidi F, Vos HJ, Mori R, de Jong N, Tortoli P. Microbubble characterization through acoustically induced deflation. IEEE Trans Ultrason Ferroelectr Freq Control 2010;57:193–202.

Harkin A, Kaper TJ, Nadim A. Coupled pulsation and translation of two gas bubbles in a liquid. J Fluid Mech 2001;445:377–411.

Howkins SD. Measurements of the resonant frequency of a bubble near a rigid boundary. J Acoust Soc Am 1965;37:504–508.

Ingard U. On the reflection of a spherical sound wave from an infinite plane. J Acoust Soc Am 1951;23:329–335.

Kinoshita M, Hynynen K. Key factors that affect sonoporation efficiency in in vitro settings: The importance of standing waves in sonoporation. Biochem Biophys Res Commun 2007;359:860–865.

Klaseboer E, Khoo BC. An oscillating bubble near an elastic material. J Appl Phys 2004;96:5808–5818.

Krasovitski B, Kimmel E. Shear stress induced by a gas bubble pulsating in an ultrasonic field near a wall. IEEE Trans Ultrason Ferroelectr Freq Control 2004;51:973–979.

Lamb H. Hydrodynamics. 6th ed. Cambridge: Cambridge University Press; 1932.

Lauterborn W. Cavitation bubble dynamics–New tools for an intricate problem. Appl Scientific Res 1982;38:165–178.

Leighton TG. The acoustic bubble. London, UK: Academic Press; 1994.

Longuet-Higgins MS. Monopole emission of sound by asymmetric bubble oscillations. Part 1. Normal modes. J Fluid Mech 1989; 201:525–542.

Marmottant P, Hilgenfeldt S. Controlled vesicle deformation and lysis by single oscillating bubbles. Nature 2003;423:153–156.

Marmottant P, Versluis M, de Jong N, Hilgenfeldt S, Lohse D. High-speed imaging of an ultrasound-driven bubble in contact with a wall: "Narcissus" effect and resolved acoustic streaming. Exp Fluids 2006;41:147–153.

Nyborg WL, Miller DL. Biophysical implications of bubble dynamics. App Sci Res 1982;38:17–24.

Ohl CD, Arora M, Ikink R, de Jong N, Versluis M, Delius M, Lohse D. Sonoporation from jetting cavitation bubbles. Biophys J 2006;91: 4285–4295.

Palanchon P, Tortoli P, Bouakaz A, Versluis M, de Jong N. Optical observations of acoustical radiation force effects on individual air bubbles. IEEE Trans Ultrason Ferroelectr Freq Control 2005;52:104–110.

Patil AV, Reynolds P, Hossack JA. A non-linear three-dimensional model for quantifying microbubble dynamics. J Acoust Soc Am 2010;127:EL80–EL86.

Plesset MS, Prosperetti A. Cavitation and bubble dynamics. Ann Rev Fluid Mech 1977;9:145–185.

Postema M, van Wamel A, Ten Cate FJ, de Jong N. High-speed photography during ultrasound illustrates potential therapeutic applications of microbubbles. Med Phys 2005;32:3707–3711.

Prentice P, Cuschieri A, Dholakia K, Prausnitz M, Campbell P. Membrane disruption by optically controlled microbubble cavitation. Nat Phys 2005;1:107–110.

Prosperetti A. Nonlinear oscillations of gas bubbles in liquids: Transient solutions and the connection between subharmonic signal and cavitation. J Acoust Soc Am 1975;57:810–821.

Qin S, Caskey CF, Ferrara KW. Ultrasound contrast microbubbles in imaging and therapy: Physical principles and engineering. Physics Med Biol 2009;54:R27–R57.

Rau KR, Quinto-Su PA, Hellman AN, Venugopalan V. Pulsed laser microbeam-induced cell lysis: Time-resolved imaging and analysis of hydrodynamic effects. Biophys J 2006;91:317–329.

Schlichting H. Boundary layer theory. 2nd ed. New York: McGraw-Hill; 1962.

Sijl J, Dollet B, Overvelde MLJ, Garbin V, Rozendal T, de Jong N, Lohse D, Versluis M. Subharmonic behavior of phospholipid-coated microbubbles. J Acoust Soc Am 2010;128:3239–3252.

Sun Y, Kruse DE, Dayton PA, Ferrara KW. High-frequency dynamics of ultrasound contrast agents. IEEE Trans Ultrason Ferroelectr Freq Control 2005;52:1981–1991.

Thomas DH, Emmer M, Vos HJ, de Jong N, Sboros V. Optical observations of microbubble oscillation in small tubes. 2009 IEEE Int Ultrason Symp Proc; P-S-11.

van der Geld CWM, Kuerten JGM. Axisymmetric dynamics of a bubble near a plane wall. J Fluid Mech 2009;640:267–305.

van der Meer SM, Dollet B, Voormolen MM, Chin CT, Bouakaz A, de Jong N, Versluis M, Lohse D. Microbubble spectroscopy of ultrasound contrast agents. J Acoust Soc Am 2007;121:648–656.

van Wamel A, Bouakaz A, Versluis M, de Jong N. Micromanipulation of endothelial cells: Ultrasound-microbubble-cell interaction. Ultrasound Med Biol 2004;30:1255–1258.

van Wamel A, Kooiman K, Harteveld M, Emmer M, ten Cate FJ, Versluis M, de Jong N. Vibrating microbubbles poking individual cells: Drug transfer into cells via sonoporation. J Control Release 2006;112:149–155.

Vos HJ, Dollet B, Bosch JG, Versluis M, de Jong N. Nonspherical vibrations of microbubbles in contact with a wall – A pilot study at low mechanical index. Ultrasound Med Biol 2008;34:685–688.

Vos HJ, Goertz DE, van der Steen AFW, de Jong N. Parametric array technique for microbubble excitation. IEEE Trans Ultrason Ferroelectr Freq Control 2011 (in press).

Wu J, Nyborg WL. Ultrasound, cavitation bubbles and their interaction with cells. Adv Drug Delivery Rev 2008;60:1103–1116.

Wu J, Ross JP, Chiu JF. Reparable sonoporation generated by microstreaming. J Acoust Soc Am 2002;111:1460–1464.

Zhao S, Ferrara KW, Dayton PA. Asymmetric oscillation of adherent targeted ultrasound contrast agents. Appl Phys Lett 2005;87:134103.

APPENDIX

PARAMETRIC STRESS MODEL

We present a model that has been developed to estimate the shear stress and the pressure exerted on a wall by an oscillating and translating neighboring bubble undergoing volumetric oscillations, translation and nonspherical deformation. It uses potential flow theory and a viscous boundary layer to calculate the stresses at the wall. Since the model could not be validated, the results should be considered as preliminary.

We made several simplifying assumptions:

(1) The wall is rigid; more precisely, its acoustic impedance is infinite. This allows to formally replace the wall by an "image bubble," namely, a fictitious bubble obtained by mirror symmetry of the real bubble with respect to the wall. This assumption is questionable, since in experiments, the wall has a finite acoustic impedance. However, the existing models of a contrast agent close to a wall have always retained the assumption of a rigid wall (Doinikov et al. 2009; Doinikov and Bouakaz 2010). Despite this limitation, these models have shown a good quantitative agreement with experiments, for instance by predicting the enhanced fundamental echo scattered by a bubble close to a wall (Doinikov et al. 2009). On the other hand, accounting for the acoustic impedance of the wall has only been proposed for an incident spherical wave (Ingard 1951),

precluding this possibility in our case, where the bubble experiences some translation and nonspherical oscillations.

(2) In agreement with our experimental results, we consider a translation only perpendicular to the wall, and the deformation is modeled up to the second axisymmetric spherical harmonic mode. Moreover, the amplitudes of translation and deformation are assumed small with respect to the amplitude of the volumetric oscillations.

(3) The flow can be described by potential flow theory, except for in a thin boundary layer located close to the wall. Such an assumption is usual in other works concerned with the effect of transient bubble motions on neighboring layers, such as laser-induced cavitation bubbles (Rau et al. 2006). To be rigorous, another boundary layer and a wake build up in the vicinity of the bubble when it starts oscillating, but we assume that these regions do not interact with the boundary layer at the wall.

(4) The wavelength is much bigger than all other relevant lengths; at a frequency $f = 2.25$ MHz and with a sound velocity $c = 1.5 \ 10^3$ m/s, the wavelength equals $\lambda = c/f = 0.7$ mm, which is indeed two orders of magnitude higher than the bubble radius and the distance of the bubble center to the wall.

(5) Gravity is neglected.

The viscous shear stress at the wall writes:

$$\tau_w(r,t) = \rho_L \nu \frac{\partial v_r}{\partial z}(r, z=0, t), \qquad (1)$$

where $\rho_L = 10^3$ kg/m^3 is the liquid density, $\nu = 10^{-6}$ m^2/s is the liquid kinematic viscosity and v_r is the velocity component parallel to the wall (see Fig. 11 for the definition of the coordinates). If the boundary layer is thin with respect to the typical scale d over which the velocity varies significantly, then v_r varies from zero at the wall (no-slip boundary condition) to the value $V(r) = \partial \Phi / \partial r(r, z=0)$, where Φ is the velocity potential. Using the classical results of the boundary layer theory (Schlichting 1962),

$$v_r(r, z, t) = \int_{-\infty}^{t} \frac{\partial V}{\partial t'}(r, t') \operatorname{erf} \frac{z}{2\sqrt{\nu(t-t')}} dt', \qquad (2)$$

where erf is the error function; inserting this expression in eqn (1) yields:

$$\tau_w(r,t) = \rho_L \sqrt{\frac{\nu}{\pi}} \int_{-\infty}^{t} \frac{\partial V}{\partial t'}(r, t') \frac{dt'}{\sqrt{t-t'}}. \qquad (3)$$

Similarly, the pressure at the wall writes (Schlichting 1962):

$$p(r,t) = -\rho_L \frac{\partial \Phi}{\partial t}(r, z=0, t) - \frac{1}{2}\rho_L V^2(r, z=0, t), \qquad (4)$$

where Φ is the velocity potential, from which these two expressions can be calculated.

We have to determine the potential flow associated with a bubble undergoing volumetric oscillations, translation, and nonspherical deformation close to a wall. This problem has been addressed by Krasovitski and Kimmel (2004) with a boundary integral method and by van der Geld and Kuerten (2009) with both an analytical and boundary integral method. We seek explicit expressions of the shear stress and pressure exerted on the wall as functions of the coefficients A_0, A_2 and of the velocity u of the center of mass, hence, the analytical method is considered. Doinikov (2001) and van der Geld and Kuerten (2009) give a general expression for the velocity potential satisfying the Laplace equation $\Delta \Phi = 0$ and the boundary condition $\partial \Phi / \partial z = 0$ at the wall, based on symmetry of the problem at the wall. However, the expression is only valid for $R < 2d$ and diverges when $\rho_L \rightarrow +\infty$, hence, cannot be used to predict the shear stress and pressure everywhere at the wall.

We use the simpler so called "method of images," *i.e.*, we superimpose the velocity potential of the real bubble in the absence of the wall with that of its image bubble (dashed shape in Fig. 11). The velocity potential is then regular at infinity, but the boundary conditions cannot be fulfilled exactly on the bubble surface, with errors appearing at second order in $R/2d$. It is, therefore, written

$$\Phi(\vec{r}) = \Phi_{\text{real}}(\vec{r}) + \Phi_{\text{image}}(\vec{r}). \qquad (5)$$
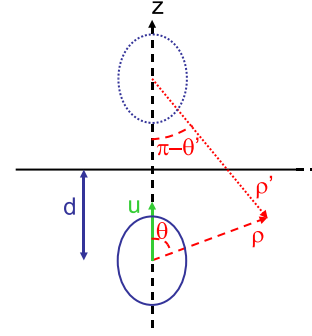

Fig. 11. Notations for the analysis of the bubble-wall interaction. The horizontal solid line represents the wall, the real bubble is sketched as an ellipse (solid line) and the image bubble with a dotted line.

The velocity potential associated with an isolated bubble undergoing volumetric oscillations, translation and nonspherical deformation in an unbound fluid has been considered by various authors (Benjamin and Ellis 1990; Feng and Leal 1995; Doinikov 2004). We take the approach of Doinikov (2004). If the bubble surface is described by the equation

$$S(\rho, \theta, t) = \rho - R(t) - \sum_{n=2}^{+\infty} A_n(t) P_n(\mu) = 0, \qquad (6)$$

where $\mu = \cos\theta$, and the velocity potential by:

$$\Phi(\rho, \theta, t) = -\frac{R^2 \dot{R}}{\rho} + \sum_{n=0}^{+\infty} a_n(t) \frac{P_n(\mu)}{\rho^{n+1}} = 0, \qquad (7)$$

where it is assumed that $|A_n| \ll R$, $|a_n| \ll R|\dot{R}|$ and $|u| \ll |\dot{R}|$, then at leading order $a_0 = 0$, $a_1 = -R^3 u/2$ and $a_n = -(2 A_n \dot{R} + \dot{A}_n R) R^{n+1} / (n+1)$. Therefore, we take the following velocity potentials:

$$\Phi_{\text{real}}(\vec{r}) = -\frac{R^2 \dot{R}}{\rho} - \frac{1}{2} R^3 u \frac{\mu}{\rho^2} - \frac{1}{3} R^3 (2 A_2 \dot{R} + \dot{A}_2 R) \frac{P_2(\mu)}{\rho^3}, \qquad (8)$$

and by mirror symmetry with respect to the wall,

$$\Phi_{\text{image}}(\vec{r}) = -\frac{R^2 \dot{R}}{\rho'} + \frac{1}{2} R^3 u \frac{\mu'}{\rho'^2} - \frac{1}{3} R^3 (2 A_2 \dot{R} + \dot{A}_2 R) \frac{P_2(\mu')}{\rho'^3}. \qquad (9)$$

Inserting eqns (8) and (9) in eqn (5) and using the geometrical relations (see Fig. 11) $\rho^2 = r^2 + (d+z)^2$, $\rho'^2 = r^2 + (d-z)^2$, $\mu = (d+z)/\rho$ and $\mu' = (z-d)/\rho$ the velocity potential becomes:

$$\Phi(r,z) = -R^2 \dot{R} \left[\frac{1}{\sqrt{r^2 + (d+z)^2}} + \frac{1}{\sqrt{r^2 + (d-z)^2}} \right]$$
$$- \frac{1}{2} R^3 u \left\{ \frac{d+z}{[r^2 + (d+z)^2]^{3/2}} + \frac{d-z}{[r^2 + (d-z)^2]^{3/2}} \right\}$$
$$- \frac{1}{3} R^3 (2 A_2 \dot{R} + \dot{A}_2 R) \left\{ \frac{2(d+z)^2 - r^2}{[r^2 + (d+z)^2]^{5/2}} + \frac{2(d-z)^2 - r^2}{[r^2 + (d-z)^2]^{5/2}} \right\}.$$

The values of $\dot{\Phi}$, V and $\dot{V}$ are computed from the experimental data. When time derivation is concerned, the relation $\dot{d} = -u$ is used. Also, second order terms of the form u^2, $A_2 u$ and their time derivatives appear that we discard since we have truncated the velocity potential at first order. After all calculations, the pressure eqn (4) becomes:

$$p(r,t) = -\rho\left\{-\frac{2\left(R^2\ddot{R}+2R\dot{R}^2\right)}{\sqrt{r^2+d^2}} - \frac{(5R^2\dot{R}u+R^3\dot{u})d}{\left(r^2+d^2\right)^{3/2}}\right.$$

$$-R^2\left(2R\ddot{R}A_2+6\dot{R}^2A_2+6R\dot{R}\dot{A}_2+R^2\ddot{A}_2\right)\frac{2d^2-r^2}{3\left(r^2+d^2\right)^{5/2}}$$

$$+2r^2\left[\frac{R^4\dot{R}^2}{\left(r^2+d^2\right)^3}+\frac{3R^5du\dot{R}}{\left(r^2+d^2\right)^4}\right.$$

$$\left.\left.+R^5\dot{R}\left(2A_2\dot{R}+\dot{A}_2R\right)\frac{4d^2-r^2}{\left(r^2+d^2\right)^5}\right]\right\}.$$

The time derivative of the velocity at the wall equals:

$$\dot{V}(r,t) = r\left[\frac{2\left(R^2\ddot{R}+2R\dot{R}^2\right)}{\left(r^2+d^2\right)^{3/2}}+\frac{3(5R^2\dot{R}u+R^3\dot{u})d}{\left(r^2+d^2\right)^{5/2}}\right.$$

$$\left.+R^2\left(2R\ddot{R}A_2+6\dot{R}^2A_2+6R\dot{R}\dot{A}_2+R^2\ddot{A}_2\right)\frac{4d^2-r^2}{3\left(r^2+d^2\right)^{7/2}}\right].$$

The shear stress eqn (3) can be calculated from the time derivative of the velocity at the wall $\dot{V}(r,t)$. However, the history kernel in eqn (3) has a factor that goes to infinity if t' approaches t. This problem was solved using the solution given by Garbin et al. (2009). The integral in eqn (3) is divided into three intervals. The first, from $-\infty$ to 0, is set to zero since it is assumed that the bubble is at rest before the arrival of the insonation pulse. The second interval ranges from 0 to $t'-\Delta t$ ($\Delta t \ll 1/f$) and the integration is carried out by a regular numerical forward integration (trapezoidal method) in MATLAB. In the final interval, $t'-\Delta t$ to t', the time derivative of V can be considered constant and the integral is approximated by $2\dot{V}\sqrt{\Delta t}$. Setting the value of $\Delta t \approx 1/(35f)$, f the insonation frequency, yielded a stable solution, and we have checked that it does not depend on the precise choice of Δt.

The double time derivations of A_0, d and A_2 enhance the high-frequency noise present in those signals. Therefore, time traces were first band-pass filtered to keep the subharmonic and fundamental frequency response, before the time derivatives were calculated.